

Minority carrier lifetimes in digitally-grown, narrow-gap, AlInAsSb alloys

Cite as: Appl. Phys. Lett. **119**, 251102 (2021); <https://doi.org/10.1063/5.0074304>

Submitted: 07 October 2021 • Accepted: 03 December 2021 • Published Online: 20 December 2021

 A. J. Muhowski,  S. D. March,  S. J. Maddox, et al.



View Online



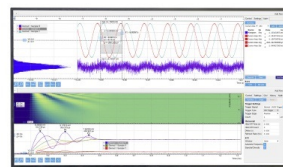
Export Citation



CrossMark

Challenge us.

What are your needs for periodic signal detection?



Zurich Instruments



Minority carrier lifetimes in digitally-grown, narrow-gap, AlInAsSb alloys

Cite as: Appl. Phys. Lett. **119**, 251102 (2021); doi: [10.1063/5.0074304](https://doi.org/10.1063/5.0074304)

Submitted: 7 October 2021 · Accepted: 3 December 2021 ·

Published Online: 20 December 2021



View Online



Export Citation



CrossMark

A. J. Muhowski,^{a)} S. D. March, S. J. Maddox, D. Wasserman, and S. R. Bank

AFFILIATIONS

Electrical and Computer Engineering Department, University of Texas, Austin, Texas 78758, USA

^{a)} Author to whom correspondence should be addressed: aaron.muhowski@utexas.edu

ABSTRACT

The minority carrier lifetime in extended-short-wavelength infrared and mid-wavelength infrared digitally-grown AlInAsSb alloys has been measured by time-resolved photoluminescence, ranging from 26 to 260 ns depending on temperature and composition. The temperature dependence of the minority carrier lifetime and the power-dependence of continuous-wave photoluminescence indicate the presence of at least two deleterious Shockley–Read–Hall recombination centers, limiting the minority carrier lifetime of AlInAsSb alloys, particularly with non-zero Al concentration.

Published under an exclusive license by AIP Publishing. <https://doi.org/10.1063/5.0074304>

Digitally-grown $\text{Al}_x\text{In}_{1-x}\text{As}_y\text{Sb}_{1-y}$ (hereafter AlInAsSb) quaternary alloys have recently emerged as a tunable III–V alloy system for low-noise avalanche photodiodes (APDs), with potential near-infrared and short-wave infrared applications in LIDAR and fiber optical communications.¹ Both conventional $p-i-n$ structures and separate absorption and charge multiplication structures have been demonstrated as well as “staircase” APDs—a long-sought class of devices that have been recently shown to exhibit greatly reduced noise characteristics beyond both conventional APDs and photomultiplier tubes.^{2–6} While most AlInAsSb development has occurred on less-mature GaSb substrates, AlInAsSb APDs have also been grown on InP substrates, presenting a path toward merging these exciting classes of devices with the more mature InP-based growth and fabrication processes.^{7–9}

Despite these device results, the basic properties of the AlInAsSb material system remain relatively unstudied. The initial explorations of random-alloy AlInAsSb showed that large portions of the compositional space were immiscible, with only sporadic reports of AlInAsSb lattice-matched to GaSb with $x > 10\%$.^{10,11} Digital growth of AlInAsSb was initially developed to circumvent the miscibility gap^{12,13} and to facilitate the use of relatively wide-gap barrier layers for InAsSb quantum well laser diodes;^{10,14,15} however, few “active” AlInAsSb devices were reported until recently. For such devices, where either absorption or emission of light occurs in an AlInAsSb layer, the minority carrier lifetime is a critical and as-yet unreported material parameter that both govern the diffusion length of minority carriers and the contribution of parasitic generation-recombination dark current in detectors as well as characterizing the defect-related, non-radiative

recombination pathways for emitters. While recent work in AlInAsSb has focused primarily on low-noise, high-gain avalanche photodiodes, AlInAsSb is also a candidate material for unity-gain photodetectors with bandgaps tunable throughout the extended-short-wavelength infrared (eSWIR) from 1.7 to $3\ \mu\text{m}$.^{16,17} At shorter wavelengths, InGaAs lattice-matched to InP serves as an ideal III–V material for infrared detection, with minority carrier lifetimes in excess of 15 μs reported.¹⁸ Lattice-matched InGaAs cannot reach longer wavelengths, where type-II superlattices are the dominant III–V material system for photodetection, with minority carrier lifetimes up to 10 μs reported.¹⁹

To this end, we report measurements of minority carrier lifetime in narrow-gap AlInAsSb alloys using time-resolved photoluminescence (PL). The temperature dependence of the minority carrier lifetimes is fit to a combination of Shockley–Read–Hall (SRH) and radiative recombination, using bandgaps determined from spectrally resolved PL. The results indicate the presence of multiple SRH trap states and greatly diminished minority carrier lifetimes for non-zero Al concentration.

Four AlInAsSb samples, with Al concentrations x of 0%, 10%, 20%, and 30%, corresponding to As concentrations y of 91%, 82%, 73%, and 64%, respectively, were grown by molecular beam epitaxy and characterized as a function of temperature. The y values were chosen, such that the films were lattice-matched to the GaSb substrate. Each sample was grown at 480 °C and had a nominal digital alloy period thickness of 10 ML and 300 nm total thickness, not including the symmetric 10 nm AlSb cladding layers for carrier confinement, which ensure that any photoluminescence can be attributed to

band-to-band processes within the AlInAsSb layer. Further details regarding the growth of these specific samples have been described thoroughly elsewhere.¹⁶ Spectrally resolved PL was excited with a pump irradiance of nominally 300 W/cm² from a laser diode emitting at 808 nm, modulated by a 10 kHz square wave. PL was collected with an all-reflective objective and directed to a liquid nitrogen cooled HgCdTe detector through a Fourier-transform infrared (FTIR) spectrometer operating in an amplitude modulation step-scan mode. Spectrally integrated, power-dependent PL measurements used the same excitation configuration and focusing the collected PL onto a liquid nitrogen cooled InSb detector. Neutral-density (ND) filters were used to control the pump power; a beam splitter and calibrated-diode power meter were used to synchronously measure the pump power. Time-resolved PL was excited using the unfocused output of a 532 nm, Q-switched Nd:YAG laser providing sub-ns pulses repeating at 20 kHz. The PL was focused onto a thermoelectrically cooled HgCdTe detector (VIGO Systems PVMI-2TE-10.6) with a <3 ns rise time. The maximum pump fluence of 19 μJ/cm² was likewise controlled using ND filters.

PL spectra at 83 and 300 K are shown for all four samples in Fig. 1. The bandgaps of the 10%–30% Al samples span the eSWIR, with the 0% sample extending further into the mid-wave infrared (MWIR, 3–5 μm). As has been noted previously, the extension to wider bandgaps for >10% Al in digitally grown has not been consistently attained in random alloy AlInAsSb as phase segregation becomes increasingly problematic beyond 10%.^{10,11} Digital growth, using short-period superlattices of the thermodynamically stable binaries (InAs, AlSb, InSb, and AlAs for AlInAsSb), has been used to grow AlInAsSb throughout the compositional space.^{10,16} The bandgaps, calculated by subtracting $k_B T/2$ from the peak PL energy for each sample at each temperature,²⁰ are shown in Fig. 1(c). A single Gaussian peak was fit to the data to extract the peak location when atmospheric absorption effects obscured the spectral maxima, such as the well-known CO₂ atmospheric absorption line at 4.2 μm. The temperature dependence of each bandgap $E_g(T)$ can be fit by the following Varshni formula:²¹

$$E_g(T) = E_g(0) - \frac{\alpha T^2}{T - \beta}, \quad (1)$$

where α and β are the Varshni parameters, $E_g(0)$ is the fitted 0 K bandgap, and T is the temperature. Least-squares fits to the measured bandgaps are also shown in Fig. 1(c), with the corresponding parameters listed in Table I.

The power-dependence of the PL can be analyzed using the Z -parameter technique.²² Here, the incident laser power I can be described as

$$I = \eta_{pump} q V_R (A \Delta n + B \Delta n^2 + C \Delta n^3), \quad (2)$$

where η_{pump} is the pumping efficiency, q is the elementary charge, V_R is the recombination volume, A is the SRH coefficient, B is the radiative coefficient, C is the Auger coefficient, and Δn is the excess carrier density. Likewise, the PL output power P can be described as

$$P = \eta_{ext} E_{ph} V_R B \Delta n^2, \quad (3)$$

where η_{ext} is the extraction efficiency and E_{ph} is the average emitted photon energy. When a single, electron–hole recombination process dominates,

$$I \propto (\sqrt{P})^Z, \quad (4)$$

and therefore,

$$Z = \frac{d(\ln I)}{d(\ln \sqrt{P})}, \quad (5)$$

where the parameter Z indicates the dominant recombination process. The $Z = 1$ and $Z = 3$ regimes can be ascribed to entirely to dominant SRH and non-degenerate Auger recombination, respectively, while the $Z = 2$ process can indicate either dominant radiative recombination or equal amounts of SRH and Auger recombination.²³

The Z parameters extracted from room-temperature and 78 K power-dependent PL are shown in Fig. 2(a). Prior to the numerical differentiation according to Eq. (5), a Savitzky–Golay filter was used to reduce noise in the curves. Half of the window length was removed from the maximum and minimum endpoints of the curves, as the Savitzky–Golay filter returns an artificially constant value. The majority of the data show Z monotonically increasing with increasing pump power, as is generally expected. Notably, the 300 K data for the 10% and 30% Al samples show a decrease in Z parameter with increasing pump power (below 10 W/cm²). Such a result would typically imply a transition from a regime with significant radiative or Auger recombination at low pump powers, to a SRH-dominated regime with increasing pump power, then finally again to radiative or Auger dominated. However, the same trend occurs when the excited carrier density

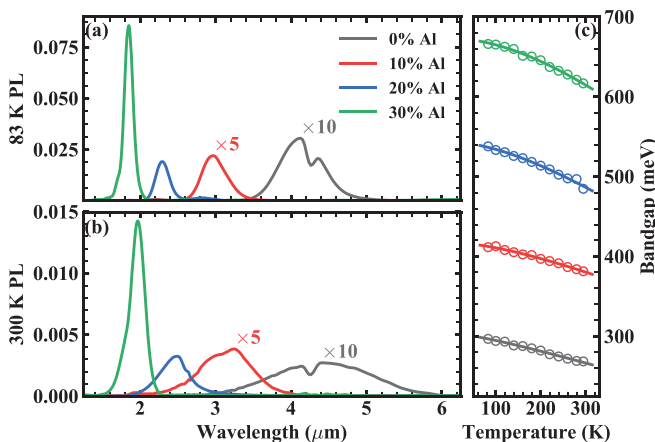


FIG. 1. (a) Spectrally resolved PL at 83 K and (b) 300 K for each of the samples. (c) The measured bandgaps (open circles) extracted from spectrally resolved PL between 83 and 300 K and Varshni fits to the data (solid lines).

TABLE I. Varshni fit parameters extracted from the data shown in Fig. 1(c).

| x (%) | $E_g(0)$ (meV) | α (meV/K) | β (K) |
|---------|----------------|------------------|-------------|
| 0 | 303 | 0.162 | 102 |
| 10 | 417 | 0.238 | 283 |
| 20 | 543 | 0.426 | 380 |
| 30 | 673 | 0.657 | 714 |

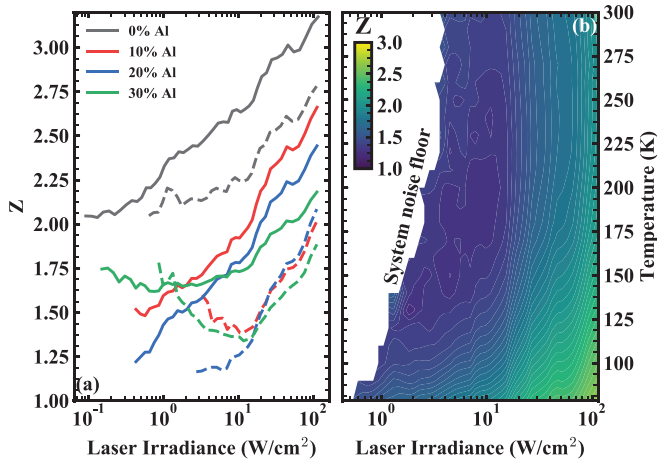


FIG. 2. (a) Calculated Z parameter as a function of pump laser irradiance for all four samples at 78 K (solid) and 300 K (dashed). (b) Calculated Z parameter as a function of temperature and pump laser irradiance for the 10% Al sample. The white space indicates PL below the system noise floor.

approaches the background carrier density. In this regime, carriers recombine at the minority carrier lifetime with density-independent SRH, radiative, and Auger contributions, and the Z parameter tends toward 2 with decreasing excitation. Therefore, the transition from decreasing Z to increasing Z occurs at the boundary between low-excitation and high-excitation regimes, with the majority of the power-dependent data occurring under high-excitation. Figure 2(b) shows a representative plot of Z parameter as a function of temperature and pump laser irradiance for the 10% Al sample. The white space corresponds to PL output below the detection limit of our PL system. The data show that the Z parameter monotonically increases with increasing pump power below 125 K. Above 125 K, however, the pump powers at which the Z minima occur begins to increase, staying at approximately 10 W/cm² above 200 K.

Time-resolved PL is a widely used technique to study carrier recombination dynamics. For our purposes, it can be used to measure the minority carrier lifetime (MCL), where the time dependence of the PL output power $P(t)$ can simply be described as

$$P(t) \propto e^{-t/\tau} \quad (6)$$

for the MCL τ . Restricting these measurements to the single-exponential, low-excitation regime relaxes some of the experimental constraints encountered in the high-excitation limit that was probed by the power-dependent measurements, shown in Fig. 2, namely, single-exponential decay generally occurs 10 ns or more after excitation, allowing sufficient time for the excited electron-hole pairs to cool to the band edge and diffuse throughout the 300 nm active region; and convolution effects between the PL decay and the detector response are minimal as the typical MCL is much longer than the detector response time (<3 ns) in the single-exponential region. These two experimental concerns, though avoided in the low-excitation regime, prevent accurate determination of the radiative rate coefficient B and the Auger coefficient C that could, otherwise, be obtained from studies at higher excitation, and likewise preclude us from estimating the quantum efficiency of these materials based on lifetime analysis. Two

PL decays, representing the longest and shortest measured MCLs presented in this work, are shown in the inset to Fig. 3(a). Each PL decay curve can be fit to Eq. (6), with single exponential behavior occurring over roughly a decade or more in PL magnitude, as seen in the inset. Note that by restricting our measurements to the single-exponential regime, we are neglecting the high-excitation data at short times after the initial excitation where the instantaneous lifetime is much faster due to contributions from radiative and Auger recombination. For example, the black curve inset to Fig. 3(a) has been fit from 240 to 700 ns to fit solely in the single-exponential regime. The fitted MCLs for each sample and temperature, ranging from 20 to 260 ns, are shown in Fig. 3(a).

Two distinct temperature dependencies of the MCL can be seen in Fig. 3(a), which can be modeled to determine the dominant recombination processes that limit the MCL. The temperature dependence of the 0% Al sample is well-fit below 200 K by SRH with saturated traps for n -type material,²⁴

$$\tau_{SRH} = \tau_{p0} = \frac{1}{\sigma_p v_p N_t} \propto T^{-1/2}, \quad (7)$$

where τ_{p0} is the characteristic hole capture time of the trap state, σ_p is the trap cross section for holes, v_p is the hole thermal velocity, and N_t is the trap density. Above 200 K, the intrinsic radiative lifetime^{25,26}

$$\tau_{rad}^i \propto e^{-E_g/2k_B T} \quad (8)$$

makes a significant contribution and eventually becomes dominant. The $E_g/2$ dependence of the exponent, using the E_g measured by spectrally resolved PL, can be used to differentiate intrinsic radiative recombination from the Auger-1 recombination process expected for n -type material (exponent $\sim E_g$) or the Auger-7 process

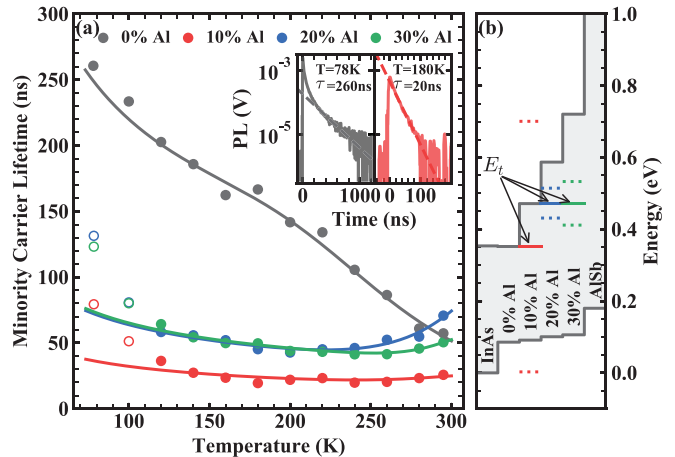


FIG. 3. (a) Minority carrier lifetimes extracted from time-resolved PL (circles), and fits to the data as described in the text. Open circles have been excluded from the fit procedure. The insets show the PL decay curves (solid) and single exponential fit (dashed) for the longest (left, 0% Al at 78 K) and shortest (right, 10% Al, 180 K) decays of 260 ns and 20 ns, respectively. (b) Gray lines represent the conduction and valence band edges of the various alloys, with the shaded regions corresponding to the bandgap. Fitted trapped energies (solid) and the associated uncertainty (dashed) are shown for the 10%, 20%, and 30% Al samples.

(exponent $\sim 2E_g$).²⁷ The Al-containing samples, however, show markedly shorter MCLs compared to the 0% sample and show neither the conventional temperature dependence associated with saturated-trap SRH or extrinsic radiative recombination nor an exponential decrease in the MCL with increasing temperature that can be ascribed to intrinsic radiative recombination or Auger recombination, again depending on the exponent. However, the MCL can be fit by the full SRH formula assuming finite occupation of the trap states:²⁴

$$\tau = \frac{\tau_{n0}(p_0 + p_1) + \tau_{p0}(n_0 + n_1)}{n_0 + p_0}, \quad (9)$$

where n_0 and p_0 are the background electron and hole densities, respectively, and n_1 and p_1 are the electron and hole densities when the Fermi energy and trap energy are equal. Equation (9) fits the Al-containing MCLs well above 100 K; the data at 100 K and below have been excluded from the fits. The low-temperature discrepancy likely arises from the interaction of multiple SRH trap states, as discussed below.

The fitted trap energies for the Al-containing samples are shown in Fig. 3(b). The SRH dependence for the 0% Al sample indicates saturated traps, and as such the trap energy does not enter the mathematical description of the SRH time, and therefore, no trap energy can be extracted. The uncertainty in the trap energy for the 10% Al sample indicates that the trap energy could be anywhere in the bandgap, so it likewise cannot be reliably extracted. The trap energies for the 20% and 30% samples are nearly equal and sit at the conduction band edge of the 10% Al sample. Energetically, the same trap states should be ineffective at mediating SRH recombination in the 0% and 10% Al samples. The temperature dependence of the MCL, nevertheless, indicates that SRH recombination is a major contribution to the total lifetime, which necessarily requires at least one additional trap state to be located within the bandgap of the 0% Al sample. Due to the relatively small change in the valence band offset with increasing x , a trap state in the bandgap of the 0% Al sample is likely to also be within the bandgap of the Al-containing samples. Further investigations to extract trap energies, via other techniques such as deep level transient spectroscopy or low-frequency noise spectroscopy, may be able to provide valuable insight into the origins of these trap states and potential strategies for their elimination or mitigation.

While the immiscibility of $x > 10\%$ AlInAsSb and concomitant lack of other MCL studies in this system prevents broad comparison, the 0% sample can be compared with random-alloy InAsSb MCLs. InAsSb lattice-matched to GaSb has exhibited minority carrier lifetimes in excess of 1 μ s, with metamorphic InAsSb of the same composition presenting similar lifetimes on GaAs and Si substrates, with MCLs over 300 ns at low temperatures.^{28–30} Deviations from the nominally ideal growth temperature of $\sim 440^\circ\text{C}$ have been shown to substantially reduce the MCL due to lower material quality.³¹ It is unclear, then, if the MCL in the digitally grown InAsSb has been impacted more by the growth temperature of 480°C , which here has been optimized for the AlInAsSb ($x \leq 70\%$) alloy system as a whole,¹⁶ or if the lower MCL is a consequence of the digital growth technique itself. The choice of 480°C for the growth temperature likely becomes more appropriate with increasing x as high-quality AlSb is typically grown at higher temperatures than InAs, and it is reasonable to expect AlInAsSb, an alloy primarily comprising InAs and AlSb when lattice-matched to GaSb, to follow this trend. However, the extracted MCLs

for the Al-containing samples are drastically lower than the digital InAsSb sample, which suggests that the inclusion of AlSb in the alloy is lowering the MCL because an intrinsic penalty to digital growth would have already been paid by the digital InAsSb sample, and 480°C is likely becoming closer to the ideal growth temperature for these alloys. The inclusion of Al in the alloys could mediate faster SRH recombination by the formation of a characteristic defect state associated with the growth process, or by widening the bandgap to include native defects associated with the constituent materials as was suggested for InAs/GaSb type-II superlattices in the MWIR.³² It is unclear from the presented data which of these is more likely and will be the subject of further investigations.

In conclusion, a multi-faceted, temperature-dependent photoluminescence study has been performed on MWIR and eSWIR, digitally-grown AlInAsSb materials. The analysis of the temperature-dependent minority carrier lifetime and power-dependent photoluminescence indicates Shockley–Read–Hall dominated recombination for AlInAsSb alloys containing any AlSb. The results suggest the presence of at least two Shockley–Read–Hall trap states, the elimination or mitigation of which may prove beneficial for AlInAsSb photodetectors operating in the eSWIR.

This work was supported by ARO (No. W911NF-17-1-0065), DARPA (No. HR0011-20-9-0087), and NSF (No. ECCS-1926187).

AUTHOR DECLARATIONS

Conflict of Interest

The authors have no conflicts to disclose.

DATA AVAILABILITY

The data that support the findings of this study are available from the corresponding author upon reasonable request.

REFERENCES

- ¹S. R. Bank, J. C. Campbell, S. J. Maddox, M. Ren, A. K. Rockwell, M. E. Woodson, and S. D. March, "Avalanche photodiodes based on the AlInAsSb materials system," *IEEE J. Sel. Top. Quantum Electron.* **24**, 3800407 (2018).
- ²M. Ren, S. J. Maddox, M. E. Woodson, Y. Chen, S. R. Bank, and J. C. Campbell, "Characteristics of $\text{Al}_x\text{In}_{1-x}\text{As}_y\text{Sb}_{1-y}$ ($x: 0.3\text{--}0.7$) avalanche photodiodes," *J. Lightwave Technol.* **35**, 2380–2384 (2017).
- ³M. E. Woodson, M. Ren, S. J. Maddox, Y. Chen, S. R. Bank, and J. C. Campbell, "Low-noise AlInAsSb avalanche photodiode," *Appl. Phys. Lett.* **108**, 081102 (2016).
- ⁴A. H. Jones, S. D. March, S. R. Bank, and J. C. Campbell, "Low-noise high-temperature AlInAsSb/GaSb avalanche photodiodes for 2- μ m applications," *Nat. Photonics* **14**, 559–563 (2020).
- ⁵S. D. March, A. H. Jones, J. C. Campbell, and S. R. Bank, "Multistep staircase avalanche photodiodes with extremely low noise and deterministic amplification," *Nat. Photonics* **15**, 468–474 (2021).
- ⁶F. Capasso, W.-T. Tsang, and G. F. Williams, "Staircase solid-state photomultipliers and avalanche," *IEEE Trans. Nucl. Sci.* **30**, 381–390 (1983).
- ⁷X. Yi, S. Xie, B. Liang, L. W. Lim, J. S. Cheong, M. C. Debnath, D. L. Huffaker, C. H. Tan, and J. P. David, "Extremely low excess noise and high sensitivity $\text{AlAs}_{0.56}\text{Sb}_{0.44}$ avalanche photodiodes," *Nat. Photonics* **13**, 683–686 (2019).
- ⁸X. Yi, S. Xie, B. Liang, L. W. Lim, X. Zhou, M. C. Debnath, D. L. Huffaker, C. H. Tan, and J. P. David, "Demonstration of large ionization coefficient ratio in $\text{AlAs}_{0.56}\text{Sb}_{0.44}$ lattice matched to InP," *Sci. Rep.* **8**, 9107 (2018).
- ⁹S. H. Kodati, S. Lee, B. Guo, A. H. Jones, M. Schwartz, M. Winslow, N. A. Pfeister, C. H. Grein, T. J. Ronningen, J. C. Campbell, and S. Krishna,

- "AllInAsSb avalanche photodiodes on InP substrates AllInAsSb avalanche photodiodes on InP substrates," *Appl. Phys. Lett.* **118**, 091101 (2021).
- ¹⁰L. G. Vaughn, L. R. Dawson, H. Xu, Y. Jiang, and L. F. Lester, "Characterization of AllInAsSb and AlGaInAsSb MBE-grown digital alloys," *Mater. Res. Soc. Symp. Proc* **744**, 72 (2003).
- ¹¹A. N. Semenov, V. A. Solov'ev, B. Y. Meltser, Y. V. Terent'ev, L. G. Prokopova, and S. V. Ivanov, "Molecular beam epitaxy of AllInAsSb alloys near the miscibility gap boundary," *J. Cryst. Growth* **278**, 203–208 (2005).
- ¹²K. Onabe, "Unstable regions in III-V quaternary solid solutions composition plane calculated with strictly regular solution approximation," *Jpn. J. Appl. Phys.* **21**, L323–L325 (1982).
- ¹³G. B. Stringfellow, "Immiscibility and spinodal decomposition in III/V alloys," *J. Cryst. Growth* **65**, 454–462 (1983).
- ¹⁴G. W. Turner, M. J. Manfra, H. K. Choi, and M. K. Connors, "MBE growth of high-power InAsSb/InAlAsSb quantum-well diode lasers emitting at 3.5 μm ," *J. Cryst. Growth* **175–176**, 825–832 (1997).
- ¹⁵L. G. Vaughn, L. R. Dawson, E. A. Pease, L. F. Lester, H. Xu, Y. Jiang, and A. L. Gray, "Type I mid-infrared MQW lasers using AllInAsSb barriers and InAsSb wells," *Proc. SPIE* **5722**, 307 (2005).
- ¹⁶S. J. Maddox, S. D. March, and S. R. Bank, "Broadly tunable AllInAsSb digital alloys grown on GaSb," *Cryst. Growth Des.* **16**, 3582–3586 (2016).
- ¹⁷D. Chen, R. Wang, J. A. McArthur, X. Xue, A. H. Jones, S. R. Bank, and J. C. Campbell, "Demonstration of infrared nBn photodetectors based on the AllInAsSb digital alloy materials system," *Appl. Phys. Lett.* **119**, 031101 (2021).
- ¹⁸R. K. Ahrenkiel, R. Ellingson, S. Johnston, and M. Wanlass, "Recombination lifetime of $\text{In}_{0.53}\text{Ga}_{0.47}\text{As}$ as a function of doping density," *Appl. Phys. Lett.* **72**, 3470 (1998).
- ¹⁹Y. Aytac, B. V. Olson, J. K. Kim, E. A. Shaner, S. D. Hawkins, J. F. Klem, M. E. Flatté, and T. F. Boggess, "Effects of layer thickness and alloy composition on carrier lifetimes in mid-wave infrared InAs/InAsSb superlattices," *Appl. Phys. Lett.* **105**, 022107 (2014).
- ²⁰A. T. Hunter and T. C. McGill, "Luminescence from HgCdTe alloys," *J. Appl. Phys.* **52**, 5779 (1981).
- ²¹Y. P. Varshni, "Temperature dependence of the energy gap in semiconductors," *Physica* **34**, 149–154 (1967).
- ²²S. J. Sweeney, A. F. Phillips, A. R. Adams, E. P. O'Reilly, and P. J. A. Thijs, "The effect of temperature dependent processes on the performance of 1.5- μm compressively strained InGaAs (P) MQW semiconductor diode lasers," *IEEE Photonics Technol. Lett.* **10**, 1076–1078 (1998).
- ²³L. L. Goddard, S. R. Bank, M. A. Wistey, H. B. Yuen, Z. Rao, and J. S. Harris, "Recombination, gain, band structure, efficiency, and reliability of 1.5- μm GaInNAsSb/GaAs lasers," *J. Appl. Phys.* **97**, 083101 (2005).
- ²⁴W. Shockley and W. T. Read, "Statistics of the recombination of holes and electrons," *Phys. Rev.* **87**, 835–842 (1952).
- ²⁵R. N. Hall, "Recombination processes in semiconductors," *Proc IEE* **106**, 923–931 (1959).
- ²⁶A. Rogalski, K. Adamiec, and J. Rutkowski, *Narrow-Gap Semiconductor Photodiodes* (SPIE, Bellingham, WA, 2000).
- ²⁷A. R. Beattie and P. T. Landsberg, "Auger effect in semiconductors," *Proc. R. Soc. A* **249**, 16–29 (1959).
- ²⁸A. Rakovska, V. Berger, X. Marcadet, B. Vinter, K. Bouzehouane, and D. Kaplan, "Optical characterization and room temperature lifetime measurements of high quality MBE-grown InAsSb on GaSb," *Semicond. Sci. Technol.* **15**, 34–39 (2000).
- ²⁹B. V. Olson, E. A. Shaner, J. K. Kim, J. F. Klem, S. D. Hawkins, L. M. Murray, J. P. Prineas, M. E. Flatté, and T. F. Boggess, "Time-resolved optical measurements of minority carrier recombination in a mid-wave infrared InAsSb alloy and InAs/InAsSb superlattice," *Appl. Phys. Lett.* **101**, 092109 (2012).
- ³⁰Z. Taghipour, A. W. K. Liu, J. M. Fastenau, D. Lubyshev, S. A. Nelson, and S. Krishna, "Investigation of bulk and surface minority carrier lifetimes in metamorphic InAsSb grown on GaAs and Si Investigation of bulk and surface minority carrier lifetimes in metamorphic InAsSb grown on GaAs and Si," *J. Appl. Phys.* **129**, 015106 (2021).
- ³¹P. Petluru, P. C. Grant, A. J. Muhowski, I. M. Obermeier, M. S. Milosavljevic, S. R. Johnson, D. Wasserman, E. H. Steenbergen, and P. T. Webster, "Minority carrier lifetime and photoluminescence of mid-wave infrared InAsSbBi Minority carrier lifetime and photoluminescence of mid-wave infrared InAsSbBi," *Appl. Phys. Lett.* **117**, 061103 (2020).
- ³²S. P. Svensson, D. Donetsky, D. Wang, H. Hier, F. J. Crowne, and G. Belenky, "Growth of type II strained layer superlattice, bulk InAs and GaSb materials for minority lifetime characterization," *J. Cryst. Growth* **334**, 103–107 (2011).